Effects of chemical randomness on strength contributors and dislocation behaviors in a BCC multi-principal element alloy

Shuang Lyu[a], Wei Li[a,b], Yuanhang Xia[a], Yue Chen[a*], Alfonso H.W. Ngan[a]

[a] Department of Mechanical Engineering, The University of Hong Kong, Pokfulam Road, Hong Kong SAR, China

[b] Department of Engineering Mechanics, Chongqing University, Chongqing 400044, China

* Corresponding author, e-mail: yuechen@hku.hk

Abstract

Molecular dynamics simulations for dislocation motion are conducted in a body centered cubic TaCrVW multi-principal element alloy (MPEA) with different chemical randomness based on a newly developed machine learning potential. The simulated critical stress for dislocation motion in samples with increasing level of randomness are analyzed in terms of three contributions: (1) Peierls stress (from 438 to 431 MPa), (2) strengthening from the average fault energy (from 261 MPa to near zero), and (3) strengthening due to local fluctuations of fault energy from the average value (from 394 to 566 MPa). As the alloy randomness increases, the Peierls stress as predicted from lattice distortion is rather invariant within the range studied, while there is a clear decreasing trend of the average fault energy and hence the associated strengthening. There is an increasing trend of strength contribution (3) as the alloy randomness increases, which offsets the decreasing trend of strength contribution (2). The overall strength of the TaCrVW alloy is therefore rather invariant within the range 964-1259 MPa with different randomness. The present work elucidates the physical basis of strength in the studied TaCrVW alloy.

Keywords

Multi-principal element alloys, Local fault-energy fluctuation, Local chemical ordering, Dislocation segments pinning.

1. Introduction

High-entropy, or multi-principal element alloys (MPEAs), have attracted extensive research interest recently due to their outstanding strength, corrosion resistance, and damage tolerance [1-5]. Refractory MPEAs composed chiefly of refractory elements, often with body-centered cubic (BCC) structure, are promising candidates for extreme-condition applications, especially in aerospace and power-generation sectors [6,7].

Instead of being an ideal random solid solution (RSS), local chemical ordering is often observed in MPEAs after thermomechanical processing both from computational simulations and experiments [8-11]. The local chemical ordering induced reduction in randomness (entropy) can influence the mobility of defects, like vacancies and dislocations, thereby affecting deformation behaviors and mechanical properties [12-14]. Most studies reported a strengthening effect of randomness decrease from extra energy consumption for ordering bond breakage [11,12,15], while softening or negligible effects have also been observed [16-18]. The underlying mechanism for the effects of randomness on strength has been attributed to the competition of reduced lattice distortion (misfit) and extra energy for order breaking, but quantitative understanding is still lacking [16]. Existing models such as that developed by Curtin and co-workers [19,20] are for high-entropy alloys in the ideal RSS state, while effects of randomness change after thermal processing on misfit and dislocation interactions have not been explicitly accounted for.

Unlike traditional BCC metals and alloys, in which screw dislocations govern plastic deformation by the kink-pair processes [21-25], the mobility of edge dislocations has been reported to be comparable to that of screw dislocations in the BCC MPEAs from nanoscale pinning processes, thereby contributing equally to strength as screw [26,27]. Moreover, an experimental study has reported a significant fraction of non-screw dislocations distributed across the entire single crystal [28]. Therefore, edge dislocation behavior in BCC MPEAs is significant and requires in-depth investigation. Dislocation morphology in MPEAs can be influenced by randomness [15,29]; in particular, we have recently shown that in a face-centered cubic (FCC) MPEA, the wavy dislocation morphology can contribute to strength [30]. However, how the randomness change influences the dislocation-waviness introduced strength is not known in BCC MPEAs.

For the above reasons, in this work we have conducted atomistic simulations to reveal the edge dislocation mobility based on a machine-learning interatomic potential, using TaCrVW as a model BCC MPEA. Randomness changes and the corresponding spatial fluctuation in the fault energy are demonstrated, as well as unusual dislocation pinning and unpinning processes. The simulated critical stress for dislocation motion is interpreted by different strength contributors including Peierls stress and fault energy effects, with the objective to understand the underlying physical basis of strength in the studied alloy.

2. Methodology

2.1 Machine-learning interatomic potential

Machine-learning has emerged recently as a tool to develop interatomic potentials with accuracy comparable to density functional theory (DFT) calculations [31]. Moment tensor potential (MTP) [32,33], with its proven balance between accuracy and computational cost [34], was used in this study for TaCrVW alloy. Two key parameters determining the potential performance, radius cutoff (R_{cut}) and maximum level (lev_{max}), were chosen as 5 Å and 20, respectively. The energy and force weights for training were set as 1 and 0.01, respectively. Detailed configuration information for training and validation data sets is given in Supplementary Note 1 [35](see also reference [36-46] therein).

The energy and force data of configurations for training were calculated from DFT using the Vienna *Ab-initio* Simulation Package (VASP) [47,48], with projector-augmented plane wave (PAW) generated pseudopotentials [49,50] and the Perdew-Burke-Ernzerh of (PBE) exchange-correlation functional [51]. The cutoff energy was set as 500 eV, and an automatic generation scheme was used to specify *k*-points a sampling spacing of about $2\pi \times 0.025$ Å^{-1}. The energy and force thresholds for self-consistency and structure relaxation were set as 10^{-6} eV and 0.01 eV/Å, respectively. A single gamma centered *k*-point mesh was used for ab initio MD calculation to generate configurations at finite temperatures, followed by accurate energy and force calculations.

2.2 Simulation cell and dislocation dynamics simulation

Simulations in this study were performed by the large-scale molecular dynamics massively parallel simulator (LAMMPS) [52], and defects were identified by the dislocation extraction algorithm (DXA) [53] and visualized via the open visualization tool (OVITO) [54]. Fig. 1 illustrates the simulation cell, with orthogonal coordinate system X = [111] ($L_X \approx 300$ Å), Y = [11$\bar{2}$] ($L_Y \approx 150$ Å), Z = [$\bar{1}$10] ($L_Z \approx 200$ Å).

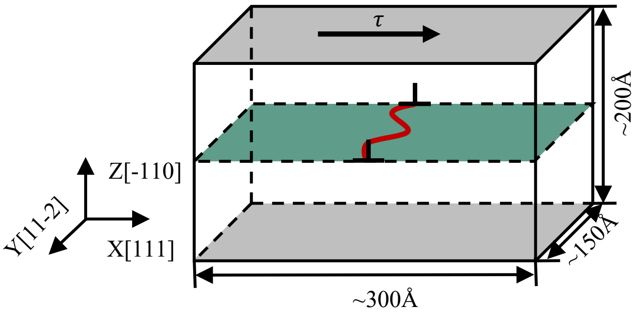

FIG. 1. Schematic illustration of MD simulation box for dislocation mobility. The red line represents a wavy dislocation; the green plane corresponds to the dislocation glide plane.

As in previous studies [16,17], periodic boundary conditions were applied in the X and Y directions, and free surface boundary condition in the Z direction. A 1/2 <111> edge dislocation was introduced to different positions of the center layer of the samples with different randomness (as described in Section 2.3). The samples with a dislocation were initially energy minimized, followed by equilibration at the target temperature for 50 ps at isothermal-isobaric (NPT) ensemble with stresses in X and Y directions relaxed. The top and bottom atom layers with thickness of 10 Å in the Z direction were fixed, and shear stress was applied to the top Z-layers. In the loading procedure, a gradually ramped loading function was used to minimize stress waves, in which the shear stress increased from zero with a rate of 50 MPa per 5 ps until reaching the target value. The applied stress was then held constant for 200 ps, and the dislocation position was recorded and analyzed.

2.3 Hybrid Monte-Carlo/molecular-dynamic (MC/MD) simulation

Configurations with different degrees of randomness were obtained from hybrid MC/MD simulations as implemented in LAMMPS package [52]. The initial structure with dimensions of $[L_X,\ L_Y, 21.7\ \text{Å}]$ was created by random substitution with the targeted atomic ratio. Periodic boundary conditions were applied in three orthogonal X-Y-Z directions, and the sample was equilibrated at the prescribed annealing temperature for 50 ps under the NPT ensemble after energy minimization, followed by the hybrid MC/MD procedure, where random exchanges of atoms with distinct species were attempted based on the Metropolis algorithm [55]. Trial runs were carried out to see the effects of different MC and MD steps per cycle, and it was found that running one MD relaxation step after ten MC swap attempts yielded results consistent with running ten MD relaxation steps after one MC swap attempt, see Fig. S.2 [35]. For the results presented below, ten MC swap attempts were performed for each MD step with a timestep of 1fs. The converged configuration was then quenched to zero temperature and duplicated along the Z ($[\bar{1}10]$) direction to create cell with size of $[L_X,\ L_Y,\ L_Z]$ for the subsequent dislocation dynamics simulation.

2.4 Local chemical ordering calculation

The Warren-Cowley (WC) order parameter [56] is used to characterize the chemical ordering of configurations from the hybrid MC/MD simulations. The chemical ordering parameter is defined as $\alpha_{\Delta \mathrm{r}}^{ij} = \frac{P_{\Delta r_{ij}}^{ij} - c_j}{\delta_{ij} - c_j}$, where $P_{\Delta \mathrm{r}}^{ij}$ is the probability of finding a *j*-type atom around an *i*-type atom in the neighbor shell Δr_{ij}, δ_{ij} is the Kronecker delta function, and c_j is the concentration of *j*-type atom. A near-zero $\alpha_{\Delta r_{ij}}^{ij}$ represents an RSS; a positive $\alpha_{\Delta \mathrm{r}}^{ij}$ for the same element pairs ($i = j$) shows segregation; negative WC parameters for different species pairs suggest cluster ordering of the two elements.

2.5 Fault energies calculation

Stacking faults were created by shifting atoms in the upper half of the simulation block relative to the lower half along X direction. Periodic boundary conditions were applied in X and Y coordinates. The global diffuse antiphase boundary energy (γ^{DAPB}) was calculated from the energy difference between the fully relaxed initial and final configurations (after displacement by one b). For the local γ_c^{DAPB} spatial distribution over the slip plane, the configuration was divided into columns along the normal direction of the $(\bar{1}10)$ slip plane with a square cross-section of 6 Å × 6 Å. The local γ_c^{DAPB} was calculated by considering the energy changes of these columns, via constrained energy minimization（relaxation only along Z direction) of the final structure to maintain conservation of atoms in each column. The slip-plane averaged value of the γ_c^{DAPB} calculated this way is a global antiphase boundary energy that is somewhat higher than the fully relaxed value γ^{DAPB} (see Table 1), because the relaxation now is constrained along the Z direction [57].

3. Results and discussion

3.1 Machine-learning interatomic potential

The interatomic potential for TaCrVW MPEA was developed based on the MTP formalism [33]. Fig. 2 presents a comparison of MTP- and DFT-predicted energies and forces for the training and testing configurations. The additional testing set, which contains stacking-fault and dislocation-dipole configurations, is used to further validate the MTP for its application to dislocation simulation. The overall root-mean-square errors (RMSEs) of the training and testing configurations (including general testing and additional testing sets) are, respectively, 2.304 meV/atom and 6.481 meV/atom for energies, and 0.088 eV/Å and 0.206 eV/Å for atomic forces.

Moreover, a comparison of the elastic constants predicted by the developed MTP and DFT can be found in Table S.1 [35], which shows high consistencies between the two methods. To further validate the reliability of the MTP before applying to dislocation simulation, the dislocation mobilities under constant shear stress in the four pure metal systems were also calculated and compared with those calculated from other potentials. The results shown in Fig. S.1 [35] indicate good consistencies with other potentials.

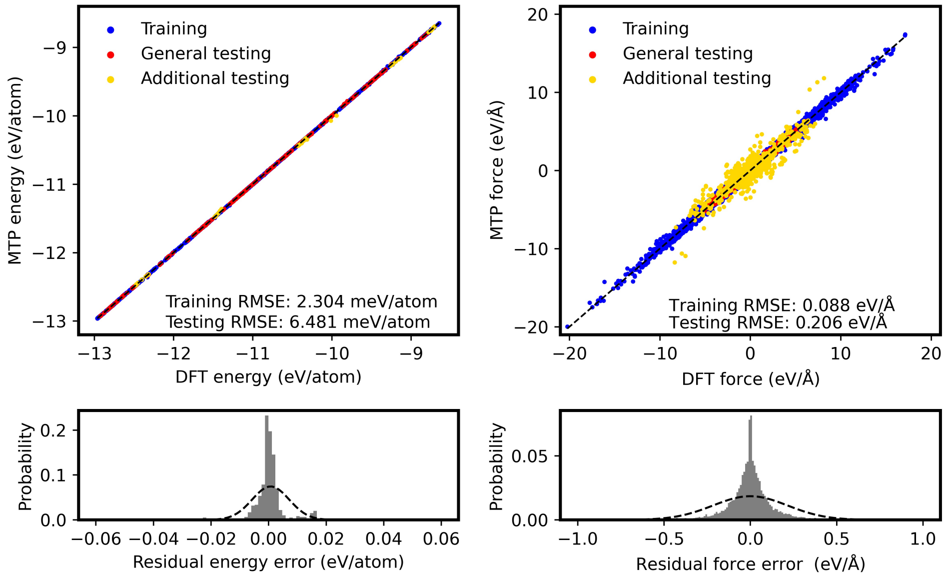

FIG. 2. Machine-learning interatomic-potential estimation. Energies and forces for training and testing configurations from DFT and MTP results are shown. The general testing set includes different AIMD and binary configurations similar to the training set; the additional testing set includes stacking-fault and dislocation-dipole configurations.

3.2 Local chemical ordering and diffuse antiphase boundary energies (γ^{DAPB})

Hybrid MC/MD calculations were first conducted from 600 K to 1800 K to obtain configurations with different degrees of randomness, and the potential energy per atom (E_p) was captured as a function of swap attempts. Fig. 3(a) presents the 800 K-annealed results, in which E_p decreases gradually with MC steps, thereby forming a more stable configuration. The E_p vs swap attempts for samples processed at other conditions can be found in Fig. S.3 [35]. The pairwise WC parameters (see Methods) in the first nearest neighbor shells， $\Delta r_{ij} = 0 \sim 2.9$ Å， are shown in Fig. 3(b). The α_1^{Ta-Cr} is negative and decreases with annealing temperature, indicating Ta-Cr ordered phase formation at a lower annealing temperature. Fig. 3(c) and (d) show atomic configurations for 600 K-annealed and RSS, respectively. The 600 K processed configuration exhibits dramatic phase separation, where obvious Ta-Cr rich regions are marked. Therefore, further dislocation dynamics simulations were only conducted for configurations annealed at 800 K and above.

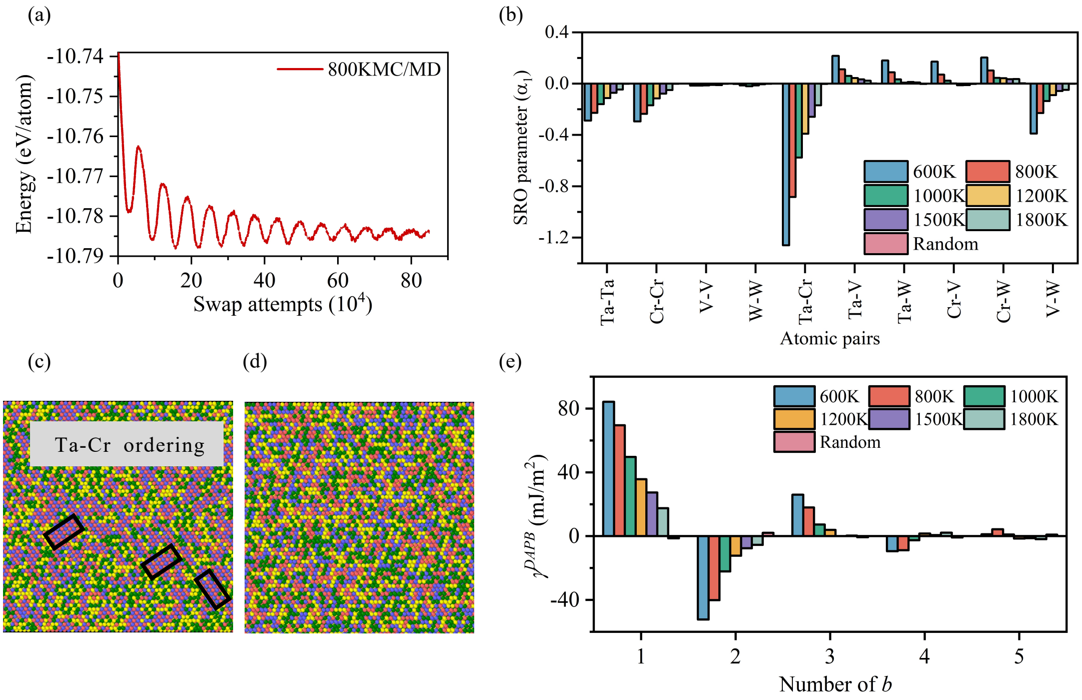

FIG. 3. Local chemical ordering for configurations annealed at different temperatures. (a) E_p vs swap attempts for 800 K annealing; (b) chemical ordering parameters at different annealing temperatures; (c) and (d) configurations (visualized by OVITO [54]) annealed at 600 K and RSS, viewed along [-110] perpendicular to slip plane; (e) Diffuse antiphase boundary energies (γ^{DAPB}) variation after several b slip for configurations annealed at different temperatures.

TABLE I. Lattice properties for samples with different randomness, including lattice constant (a), elastic constants (C_{11}, C_{12}, C_{44}), Zener's anisotropy ratio (A), shear modulus (μ), Poisson's ratio (ν), and diffuse antiphase boundary energy (γ^{DAPB} from full relaxation, and γ_c^{DAPB} from constrained relaxation).

Properties	Annealing Temperature (K)						Random
	600	800	1000	1200	1500	1800	
a [Å]	3.0995	3.1001	3.1007	3.1009	3.1012	3.1013	3.1035
C_{11} [GPa]	393.5	390.5	386.0	383.5	381.7	379.9	378.3
C_{12} [GPa]	151.3	153.9	155.3	155.9	156.1	156.2	157
C_{44} [GPa]	60.7	60.3	60.0	59.7	59.7	59.4	60.2
A	0.50	0.51	0.52	0.52	0.53	0.53	0.54
μ [GPa]	85.8	84.5	83.2	82.4	82.1	81.5	81.7

n	0.345	0.347	0.349	0.350	0.350	0.350	0.350
γ^{DAPB}[mJ/m^2]	84	70	50	36	27	18	-1 (~0)
γ_c^{DAPB}[mJ/m^2]	101	89	75	63	56	47	33

Table I lists the bulk properties for samples annealed at different temperatures. The lattice constant decreases slightly as the annealing temperature and randomness decreases. The γ^{DAPB} for the first b slip increases from near zero for the random system to 84 mJ/m^2 for the 600 K-processed configuration, as shown in Table 1 and Fig. 3(e), which can be attributed to the extra energy consumption for ordering-bond destruction across the slip plane for more ordered systems. Specifically, the negative γ^{DAPB} for the second b slip for the lower-temperature annealed samples can be understood by the restoration of the more stable local ordering phase. Moreover, γ^{DAPB} vanishes with repeated shears by b on the same slip plane, as shown in Fig. 3(e), which indicates that five successive shears by b can break the local chemical ordering between the atomic layers across the glide plane, in consistence with a previous investigation [15].

3.3 Pinning and unpinning mechanism of dislocation segments

Fig. 4(a) shows a series of dislocations extracted every 2 ps from the MD simulation. The lines are severely curved and do not move smoothly due to the inhomogeneous local environment. Some regional segments can slip forward, while others are quasi-static because of insufficient energy obtained to conquer the local obstacles. Local traps pin the immobile segments, thereby line length will increase by bowing and energy is gained from the external stress. Dislocation segments will be unpinned until enough energy is obtained to overcome the local resistance, considerably different from the smooth movement of straight dislocations in pure metallic systems [26,58].

Local γ_c^{DAPB} is used to examine the influence of local fault-energy fluctuation on the pinning of dislocation segments. The spatial variation and statistical distribution of the local γ_c^{DAPB} over the glide plane for the RSS sample are plotted in Fig. 4(a) and (b), respectively. From Fig. 4(a), the local γ_c^{DAPB} exhibits severe fluctuation, with some local regions exhibiting γ_c^{DAPB} values as high as 400 mJ/m^2. As we have analyzed recently [30], such regions of high local γ_c^{DAPB} are potential pinning sites for dislocations motion since gliding across them would be accompanied by local high faulting energy barriers, and here, we provide evidence for this in the present alloy. Due to the trapping processes, the velocities of different segments along the same dislocation vary. To identify the pinning sites, local velocities along dislocations are estimated, and segments with a local velocity lower than 1 Å/ps are captured as pinning sites. For instance, Fig. 4(c) shows five dislocations extracted from Fig. 4(a), and the corresponding local velocities are illustrated in Fig. 4(d). After mapping the local velocities and positions to the spatial distribution of local γ_c^{DAPB} on the slip plane, we can obtain the local γ_c^{DAPB} at the pinned regions. Fig. 4(b) shows a comparison of the γ_c^{DAPB} statistic distribution over the whole glide plane and at pinning sites for the RSS state; it can be seen that the mean γ_c^{DAPB} at the pinning sites μ_p= 73.02 mJ/m^2 is higher than the mean μ_t= 33.26 mJ/ m^2 for the whole glide plane. For the alloys processed at other conditions, the same trends are observed as shown in Fig. S.4 [35].

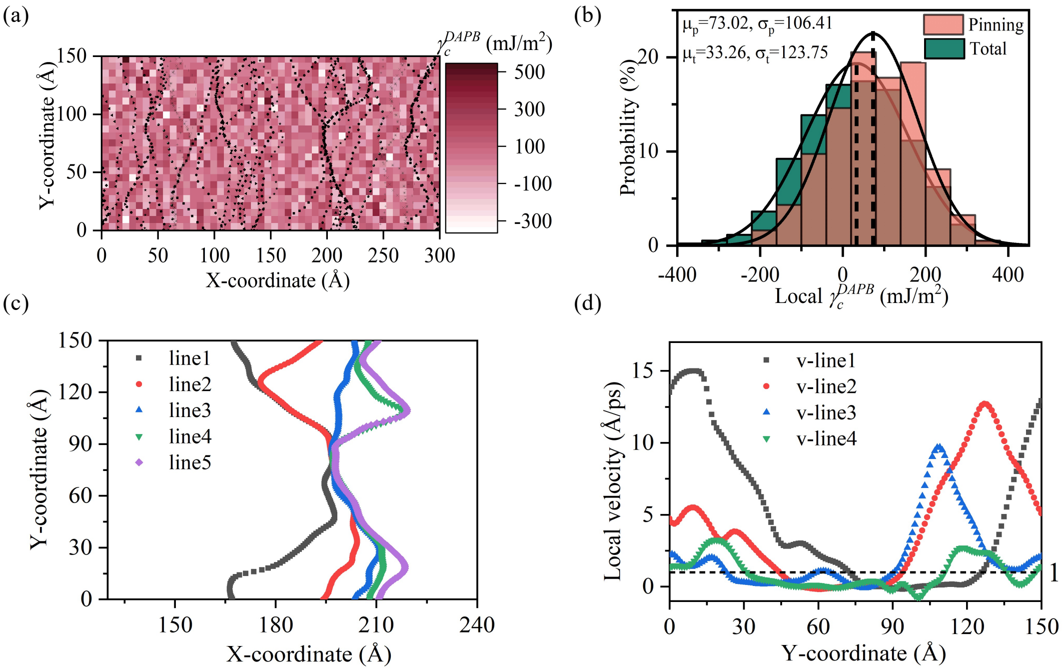

FIG. 4 Dislocation motion accompanied by local pinning and unpinning. (a) Curved dislocations as superimposed onto the spatial distribution map of local γ_c^{DAPB} over the glide plane in RSS; (b) statistical distribution of local γ_c^{DAPB} over the whole glide plane and at pinning sites, with mean values μ and standard deviations σ; (c)-(d) illustrate several dislocations and their local velocities.

3.4 Critical shear stress for dislocation motion

The critical shear stress (CRSS) for the entire dislocation line to glide continuously across the slip plane as a function of the annealing temperature is shown in Fig. 5. Different from most previous studies that randomness decrease can result in strengthening [15,30], the average CRSS in the TaCrVW alloy at 5 K varies from 964 MPa to 1259 MPa for samples with different levels of randomness. Moreover, for a sample with finite randomness, the CRSS calculated from five independent MD simulations (with initial dislocations located at five different positions of the slip plane) scatter significantly, as shown in Fig. 5. Note that a softening behavior of edge dislocations in an 800 K-annealed MoNbTaW sample has been reported previously [16], and the mechanism was attributed to a competition between the improved strength resulting from the increasing in ordering degree and reduced strength arising from the decreasing of lattice friction compared with the random state. However, no quantitative evidence has been given for such a conjecture; thus, in-depth investigation on the different strength contributions is essential to reveal the underlying mechanism.

The CRSS and the corresponding standard deviations at 300 K for the first slip of dislocation (dislocation glides across the slip plane for the first time), and at 5 K for the fifth slip (dislocation glides across the slip plane repeatedly for the fifth time, so the ordering across the glide plane has been destroyed), are also illustrated in Fig. 5. The average CRSS calculated at 300 K for samples of different randomness shows a similar trend but with reduced values compared with the 5 K first slip results. The average CRSS for dislocation multi-slip decreases gradually as the sample randomness decreases. An increment of the CRSS for the 1800 K-annealed sample for multi-slip compared with first slip, and a decrease or invariance for other samples can be noted. From Fig. 3(e), the generalized γ^{DAPB} vanishes after five successive passes of the dislocation, which indicates a decrease in strength contribution from the generalized γ^{DAPB} compared with the first slip. Therefore, considering the elevated strength for the multi-slip for the 1800 K-annealed samples, there should be other strengthening factors after the breakage of ordering bonds, which will be discussed in Section 4 below.

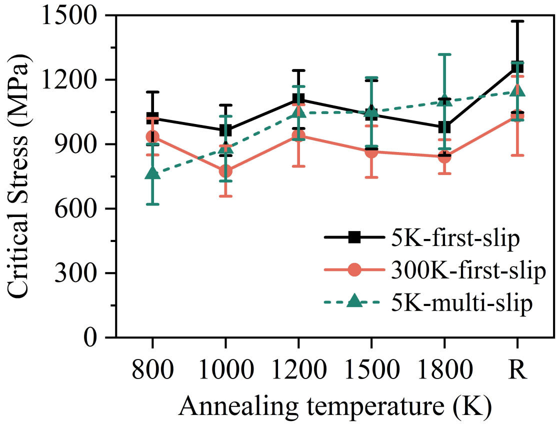

FIG. 5 Critical shear stress for configurations processed at different conditions, at 5 K and 300 K for the first slip, and 5 K for the fifth slip. R denotes random solid solution. Error bars correspond to the standard deviations of each data point.

4. Competing contributions to strength

To explain the variation of strength with the annealing condition in Fig. 5, we analyze the effects of randomness on the intrinsic Peierls stress of the alloy, as well as on the strength arising from the global γ^{DAPB} and its local fluctuations.

4.1 Effects of randomness on Peierls stress strengthening

First, we consider the Peierls stress, and in particular, how this is influenced by the lattice distortion introduced by the randomness of the alloy. The Peierls stress is given as [59,60]:

$$\tau_p^0 = \frac{2\mu}{1-\nu} \exp\left[-\frac{2\pi d}{b}\right] \tag{1}$$

where μ is shear modulus, ν is Poisson's ratio, b is Burger's vector and d is the interplanar spacing. When applied to an MPEA, the length scales b and d will be affected by the lattice distortion of the alloy, and 1.02 is used here for $\frac{d}{b}$. Fig. S.5(a) shows the distribution of the change of the Voronoi volume, ΔV, relative to the volume V_p of the perfect Voronoi cell without lattice distortion, as computed from structures after annealing. It can be seen that the standard deviation ΔV increases from 0.35 for the 800 K-annealed sample to 0.53 for the RSS state. To examine how the lattice distortion may affect the Peierls stress, we modify a model developed by Zhang et al. [61], in which stochasticity is introduced into the Peierls stress by scaling the stacking-fault energy (SFE) with a random variable. Here, the effect of the SFE fluctuation will be dealt with separately as another strength contribution (see section 4.2 below), and for the Peierls stress, we consider that randomness is introduced into the length scales b and d in eqn. (1), which can be related to the fluctuation of the Voronoi cell volume as observed in Fig. S.5. Considering that the primitive cell of the crystal is a rectangular block of volume $V = b^2 d$, where b^2 is the area on the slip plane, and d is the interplanar spacing of the slip plane, when expressed in units of b^3 the Voronoi cell volume is $V/b^3 = d/b$. As lattice distortion exists, Voronoi cell volume should fluctuate, which can be represented by scaling d/b by a random variable ω drawn from the normal distribution of mean 1 and standard deviation Δ, i.e.

$$\omega \frac{d}{b} \rightarrow \frac{d}{b} \tag{2}$$

On substituting eqn. (2) into eqn. (1), the Peierls stress becomes $\tau_p^* = \frac{2\mu}{1-\nu} \exp\left[-\frac{2\pi d}{(1-\nu)b}\omega\right]$, the mean value of which is

$$\langle \tau_p^* \rangle = \int_0^\infty \tau_p^*(\omega)\, P_\omega(\omega) d\omega = \tau_p^0 \times \langle \tilde{\tau}_p^* \rangle, \tag{3}$$

where $P_\omega(\omega) = \frac{1}{\Delta\sqrt{2\pi}} \exp\left[-\frac{(\omega-1)^2}{2\Delta^2}\right]$ is the normal distribution of ω with mean 1 and standard deviation Δ. In eqn. (3),

$$\langle \tilde{\tau}_p^* \rangle = \frac{1}{\Delta\sqrt{2\pi}} \int_0^\infty \exp\left[-\frac{2\pi d(\omega-1)}{b(1-\nu)} - \frac{(\omega-1)^2}{2\Delta^2}\right] d\omega \tag{4}$$

is a normalization factor that depends on Δ, ν and (d/b). For simplicity, Δ here is taken to be the $\Delta V/V_p$ obtained from the distributions of the Voronoi-volume change shown in Fig. S.5 [35]. Then, as Δ increases from 0.028 for the 800 K-annealed sample to 0.037 for the RSS, with the values of μ and ν taken from Table 1, the corresponding Peierls stress changes only slightly from 438 MPa to 431 MPa, as randomness in the alloy increases. This is because, as shown in Fig. S.5(b) [35], the factor $\langle \tilde{\tau}_p^* \rangle$ actually does not change significantly from 1 when the lattice distortion Δ changes within the range from 0.028 to 0.037 for the present alloy system; instead, the slight changes in the Peierls stress are due to the slight reduction in μ as randomness increases (Table 1), while the variation Δ in the lattice distortion does not constitute a significant factor to change the Peierls stress.

4.2 Effects of randomness on fault energy strengthening

We have recently investigated the effects of ordering on strengthening due to fault energy for an FCC MPEA [30], and here, we apply this model to elucidate the strengthening mechanism of the present TaCrVW alloy. In this model, the fault energy offers two types of strength contributions. First, strengthening arises from the diffuse antiphase boundary generated in the wake of a moving dislocation, the energy of which, the global γ^{DAPB}, varies with randomness as shown in Fig. 3(e) for the present alloy. Secondly, as mentioned above, the local regions on the slip plane with higher-than-average γ_c^{DAPB} are potential pinning sites; hence a dislocation traversing in a field of such pinning sites will continuously adopt different wavy shapes as depicted in Fig. 6(a), and hence its line-tension energy will fluctuate to give rise to a strength contributor. By considering energy balance, the sweep distance $w(y)$ between two successive wavy states (which are not necessarily equilibrium states) satisfies [30],

$$\tau_\gamma b \int_0^L w(y)\, dy = \frac{T}{2}\int_0^L [w'(y)]^2\, dy + \int_0^L \left(\int_0^{w(y)} \gamma(x,y)\, dx\right) dy \tag{5}$$

where $\gamma(x,y)$ is the spatial distribution of local fault energy, $T=\alpha\mu b^2$ is the line tension of the dislocation with α dependent on the dislocation character, and μ is the shear modulus. In eqn. (5), τ_γ is the fault-introduced resistance stress, and $\tau_\gamma b = f_a - f_f$, where f_a and f_f are respectively the force on unit length of dislocation due to the applied stress and Peierls stress. As discussed above, the $\gamma(x,y)$ may be written as $\gamma(x,y) = \bar{\gamma} + \Delta\gamma(x,y)$ where $\bar{\gamma}$ is the global average $\gamma(x,y)$ (the quantity listed in Table 1), and $\Delta\gamma(x,y)$ is the fluctuating part that results in wavy dislocations. Then, the fault introduced resistance can be decomposed into two parts as $\tau_\gamma = \tau_{\bar{\gamma}} + \tau_{\Delta\gamma}$, where

$$\tau_{\bar{\gamma}} = \bar{\gamma}/b \tag{6}$$

is the resistance stress due to the average γ^{DAPB} ($\bar{\gamma}$), and $\tau_{\Delta\gamma}$ is that due to the fluctuations of γ_c^{DAPB} given by

$$\tau_{\Delta\gamma} \approx \frac{T}{2b}\frac{\int_0^L [w'(y)]^2\, dy}{\int_0^L w(y)\, dy} \tag{7}$$

To calculate $\tau_{\Delta\gamma}$ from eqn. (7), wavy snapshots of a travelling dislocation were captured from the MD simulation and the sweep distance $w(y)$ between two successive snapshots was calculated and fitted to an N-degree Fourier series

$$w(y) = \lambda_0 + \sum_{i=1}^{N} \lambda_i \sin\left(\frac{2\pi y}{\ell_i} + \phi_i\right) \tag{8}$$

Then, eqn. (7) will take the form [30]:

$$\tau_{\Delta\gamma} \approx \frac{\alpha\mu b\pi^2 \sum_i {k_i}^2}{\lambda_0} \tag{9}$$

where $k_i = \lambda_i/\ell_i$ is for the Fourier harmonics. Eqn. (9) then enables $\tau_{\Delta\gamma}$ to be calculated.

4.3 Strength contributors

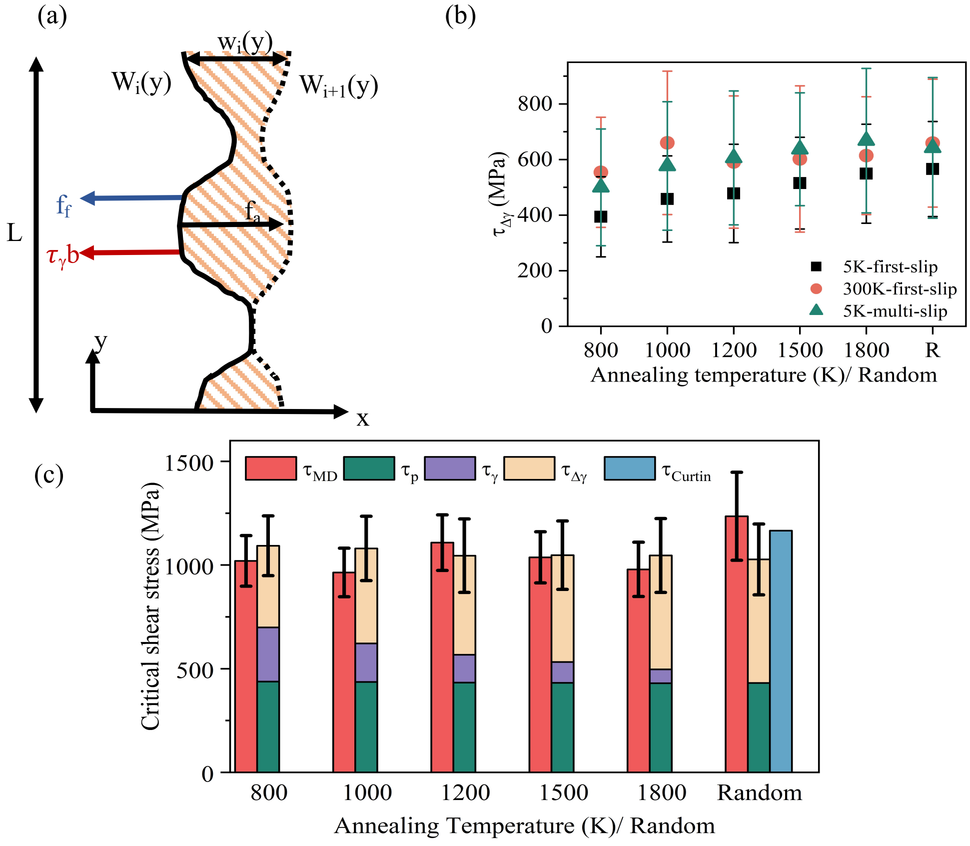

FIG. 6. Theoretical analysis of critical stress for dislocation motion. (a) Schematic diagram showing forces acting on a wavy dislocation shape $W_i(y)$ and its next position $W_{i+1}(y)$, with sweep distance of $w_i(y)$ in between. f_a, f_f and $\tau_\gamma b$ are force induced by the applied stress, Peierls stress and stacking-fault introduced resistance, respectively; (b) resistance stress due to fault-energy fluctuations ($\tau_{\Delta\gamma}$) for the first and fifth slip by ½[111] across the glide plane; (c) comparison of MD calculated critical stress (τ_{MD}) and theoretical estimates of different strength contributions (τ_p = Peierls stress, $\tau_\gamma = \bar{\gamma}/b$ is the stress from average γ^{DAPB} , and $\tau_{\Delta\gamma}$ is the stress from fault-energy fluctuations) for different condition processed samples. For RSS, Curtin's theoretical model is also presented as a comparison. Error bars correspond to the standard

deviations of each data point.

Fig. 6(c) shows the estimated values of the different strength contributors. First, the Peierls stress τ_p remains almost constant at around 431-438 MPa for the samples with different randomness. Then, the $\tau_{\bar{\gamma}}$ calculated from $\bar{\gamma}$ (γ^{DAPB}) in Table 1 exhibits a rise as the randomness decreases, e.g., 67 MPa and 261 MPa for the 1800 K and 800 K-annealed sample, respectively.

Finally, the $\tau_{\Delta\gamma}$ resistance was calculated from eqn. (9). Sweep distance w(y) is obtained from the difference between two neighbouring line states W_{j+1}-W_j, after which 8-degree Fourier fitting was conducted for w(y) to obtain the k_i and λ_0 parameters in eqn. (9). Using μ in Table 1, b calculated from the lattice constant, and $\alpha = 0.125$ [19,20], a series of $\tau_{\Delta\gamma}$ were obtained, and the average value and standard deviation in each state are shown in Fig. 6(b). As is similar to the scatter of the MD calculated CRSS, the $\tau_{\Delta\gamma}$ also scatters significantly. The average $\tau_{\Delta\gamma}$ for the first-slip at 5 K simulation increases from 394 MPa for the 800 K-annealed sample to 566 MPa for the random state. Interestingly, the increase of $\tau_{\Delta\gamma}$ with randomness almost balances out the decrease of $\tau_{\bar{\gamma}}$, thus, leading to the small variation of the final critical stress. Moreover, from Fig. 6(b), the average $\tau_{\Delta\gamma}$ for the fifth slip at 5 K and first slip at 300 K are both higher than the 5 K first slip results. These findings indicate that randomness (entropy) increase can contribute to the rise of $\tau_{\Delta\gamma}$ by affecting the dislocation morphology.

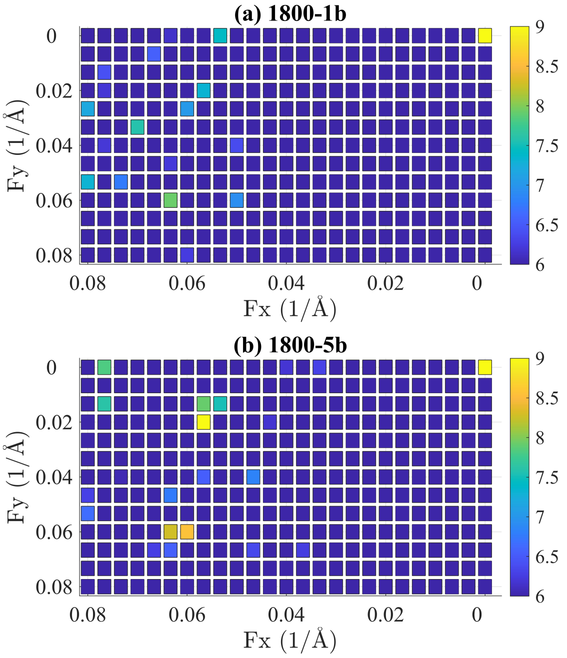

FIG. 7. Comparison of 2D FFT distribution of the local γ_c^{DAPB} map for first and fifth slip by ½ [111] across the glide plane. Fx and Fy denote frequencies in X and Y directions.

To further validate the last point, we performed two-dimensional fast Fourier transform (2D FFT) of the local γ^{DAPB} map to reveal its harmonics, from which we can obtain information about the FFT peaks and their locations in the reciprocal space, which are strengthening factors. Fig. 7(a) and (b) compare the 2D FFT results for the local γ^{DAPB} map for the first and fifth slip for the 1800 K annealed sample, from which it can be seen that stronger peaks are present in the fifth slip sample, which has higher entropy due to the destroyed ordering. These peak values reflect strong pinning sites, which can result in higher waviness of the dislocations, thus leading to higher $\tau_{\Delta\gamma}$. For samples with other randomness, similar observations can be made, as shown in Fig. S.6 [35].

Taking the above three contributions together, comparison with the MD results is made in Fig. 6(c), with discrepancies lower than $\pm 20\%$. As mentioned above, $\tau_{\Delta\gamma}$ and $\tau_{\bar{\gamma}}$ show an apparent opposite relationship with chemical randomness, while τ_p exhibits an almost constant value. For the ideal RSS, $\tau_{\Delta\gamma}$ reaches 566 MPa, which takes up more than half of the total strength, while for the 800 K-processed sample, the three components all make significant contributions.

In addition, Curtin et al.'s model [20], which considers line tension and misfit, is also used in the comparison for the ideal RSS state:

$$\tau_{curtin} = 0.04\alpha^{-\frac{1}{3}}\bar{\mu}\left(\frac{1+\nu}{1-\bar{\nu}}\right)^{\frac{4}{3}}\left[\frac{\sum_n c_n \Delta V_n^2}{\bar{b}^2}\right]^{\frac{2}{3}} \tag{10}$$

Here, $\bar{\mu} = \sqrt{\frac{1}{2}C_{44}(C_{11}-C_{12})}$ is the isotropic shear modulus, ν is the Poison's ratio, $\bar{b}$ is the Burgers vector, and $\Delta V_n = V_n - \bar{V}$ is the volume misfit, where V_n is the atomic volume for metal n, $\bar{V}$ is calculated from Vegard's law. The calculated strength from this model, τ_{curtin}, is 1166 MPa, as illustrated in Fig. 6(c), which agrees reasonably with the MD simulation (1259 MPa) and theoretical prediction (1027 MPa) in this study.

Summary

In summary, we developed a new machine-learning interatomic potential for a BCC TaCrVW refractory MPEA and applied it to dislocation dynamics study over a wide range of randomness. An analytical model considering the Peierls stress, generalized fault energy and its fluctuation induced resistance is developed. With randomness decreasing, the strength introduced by the average fault energy rises, while local fault energy fluctuation produces less wavy dislocations thus contributing less to the total strength. The opposite trends of strengthening due to the average and fluctuation of the fault energy fortuitously cancel out, thus the final critical stress exhibits little variance for samples with different randomness. These findings demonstrate the unique strengthening mechanism in MPEAs with different randomness.

Acknowledgement

This work is supported by the National Key Research and Development Program of China (2019YFA0209904). The authors are grateful for the research computing facilities offered by ITS, HKU. W L also acknowledges support from the National Natural Science Foundation of China (Nos. 12102069 and 11932004).

Data availability

The training, testing configurations, and the trained potential are available in open repository (https://github.com/shuanglyu3/TaCrVW-potential).

References

[1] O. El-Atwani, N. Li, M. Li, A. Devaraj, J. K. S. Baldwin, M. M. Schneider, D. Sobieraj, J. S. Wrobel, D. Nguyen-Manh, S. A. Maloy, and E. Martinez, Sci Adv **5**, eaav2002 (2019).

[2] Y. Zhang, G. M. Stocks, K. Jin, C. Lu, H. Bei, B. C. Sales, L. Wang, L. K. Beland, R. E. Stoller, G. D. Samolyuk, M. Caro, A. Caro, and W. J. Weber, Nat Commun **6**, 8736 (2015).

[3] S. Zhao, Y. Xiong, S. Ma, J. Zhang, B. Xu, and J.-J. Kai, Acta Materialia **219** (2021).

[4] E. P. George, D. Raabe, and R. O. Ritchie, Nature Reviews Materials **4**, 515 (2019).

[5] W. Li, H. Fan, J. Tang, Q. Wang, X. Zhang, and J. A. El-Awady, Materials Science and Engineering: A **763** (2019).

[6] O. Senkov, G. Wilks, D. Miracle, C. Chuang, and P. Liaw, Intermetallics **18**, 1758 (2010).

[7] O. N. Senkov, D. B. Miracle, K. J. Chaput, and J.-P. Couzinie, Journal of materials research **33**, 3092 (2018).

[8] X. Chen, Q. Wang, Z. Cheng, M. Zhu, H. Zhou, P. Jiang, L. Zhou, Q. Xue, F. Yuan, J. Zhu, X. Wu, and E. Ma, Nature **592**, 712 (2021).

[9] E. Antillon, C. Woodward, S. I. Rao, and B. Akdim, Acta Materialia **215** (2021).

[10] B. Zhang, J. Ding, and E. Ma, Applied Physics Letters **119** (2021).

[11] X. Yang, Y. Xi, C. He, H. Chen, X. Zhang, and S. Tu, Scripta Materialia **209** (2022).

[12] R. Zhang, S. Zhao, J. Ding, Y. Chong, T. Jia, C. Ophus, M. Asta, R. O. Ritchie, and A. M. Minor, Nature **581**, 283 (2020).

[13] F. Zhang, S. Zhao, K. Jin, H. Xue, G. Velisa, H. Bei, R. Huang, J. Ko, D. Pagan, and J. Neuefeind, Physical Review Letters **118**, 205501 (2017).

[14] S. Lyu and Y. Chen, Materials Today Communications **33**, 104485 (2022).

[15] Q. J. Li, H. Sheng, and E. Ma, Nat Commun **10**, 3563 (2019).

[16] S. Yin, Y. Zuo, A. Abu-Odeh, H. Zheng, X. G. Li, J. Ding, S. P. Ong, M. Asta, and R. O. Ritchie, Nat Commun **12**, 4873 (2021).

[17] E. Antillon, C. Woodward, S. I. Rao, B. Akdim, and T. A. Parthasarathy, Acta Materialia **190**, 29 (2020).

[18] B. Yin, S. Yoshida, N. Tsuji, and W. A. Curtin, Nat Commun **11**, 2507 (2020).

[19] C. Varvenne, A. Luque, and W. A. Curtin, Acta Materialia **118**, 164 (2016).

[20] F. Maresca and W. A. Curtin, Acta Materialia **182**, 235 (2020).

[21] J. Chaussidon, M. Fivel, and D. Rodney, Acta materialia **54**, 3407 (2006).

[22] J. Marian, W. Cai, and V. V. Bulatov, Nature materials **3**, 158 (2004).

[23] A. Ngan and M. Wen, Computational Materials Science **23**, 139 (2002).

[24] M. Wen and A. Ngan, Acta materialia **48**, 4255 (2000).

[25] A. Ngan and H. Zhang, Mechanics of Materials **31**, 367 (1999).

[26] B. Chen, S. Li, H. Zong, X. Ding, J. Sun, and E. Ma, Proc Natl Acad Sci U S A **117**, 16199 (2020).

[27] D. Yang, B. Chen, S. Li, X. Ding, and J. Sun, Materials Science and Engineering: A **855** (2022).

[28] F. Wang, G. H. Balbus, S. Xu, Y. Su, J. Shin, P. F. Rottmann, K. E. Knipling, J. C. Stinville, L. H. Mills, O. N. Senkov, I. J. Beyerlein, T. M. Pollock, and D. S. Gianola, Science **370**, 95 (2020).

[29] R. Zhang, S. Zhao, C. Ophus, Y. Deng, S. J. Vachhani, B. Ozdol, R. Traylor, K. C. Bustillo, J. Morris Jr, and D. C. Chrzan, Science Advances **5**, eaax2799 (2019).

[30] W. Li, S. Lyu, Y. Chen, and A. H. Ngan, Proceedings of the National Academy of Sciences **120**, e2209188120 (2023).

[31] V. L. Deringer, M. A. Caro, and G. Csányi, Advanced Materials **31**, 1902765 (2019).

[32] A. V. Shapeev, Multiscale Modeling & Simulation **14**, 1153 (2016).

[33] I. S. Novikov, K. Gubaev, E. V. Podryabinkin, and A. V. Shapeev, Machine Learning: Science and Technology **2**, 025002 (2020).

[34] Y. Zuo, C. Chen, X. Li, Z. Deng, Y. Chen, J. Behler, G. Csanyi, A. V. Shapeev, A. P. Thompson, M. A. Wood, and S. P. Ong, J Phys Chem A **124**, 731 (2020).

[35] See Supplementary Information at (URL) for the detailed training and testing sets for the potential development; potential energy convergence during hybrid MC/MD simulation; statistic distribution of local diffuse antiphase boundary energy; Peierls stress contributor calculation; two-dimensional fast Fourier transform (2D FFT) of local DAPB map. The Supplementary Information also contains Refs. [36-46].

[36] X.-G. Li, C. Chen, H. Zheng, Y. Zuo, and S. P. Ong, npj Computational Materials **6** (2020).

[37] An exploration of the grain boundaries, surfaces, and Wulff shapes of the elements, http://crystalium.materialsvirtuallab.org

[38] W. S. Morgan, G. L. Hart, and R. W. Forcade, Computational Materials Science **136**, 144 (2017).

[39] G. L. Hart, L. J. Nelson, and R. W. Forcade, Computational Materials Science **59**, 101 (2012).

[40] G. L. Hart and R. W. Forcade, Physical Review B **77**, 224115 (2008).

[41] A. Van De Walle, M. Asta, and G. Ceder, Calphad **26**, 539 (2002).

[42] A. Zunger, S.-H. Wei, L. Ferreira, and J. E. Bernard, Physical Review Letters **65**, 353 (1990).

[43] R. Ravelo, T. Germann, O. Guerrero, Q. An, and B. Holian, Physical Review B **88**, 134101 (2013).

[44] P. A. Olsson, Computational materials science **47**, 135 (2009).

[45] M.-C. Marinica, L. Ventelon, M. Gilbert, L. Proville, S. Dudarev, J. Marian, G. Bencteux, and F. Willaime, Journal of Physics: Condensed Matter **25**, 395502 (2013).

[46] C. Howells and Y. Mishin, Modelling and Simulation in Materials Science and Engineering **26**, 085008 (2018).

[47] G. Kresse and J. Hafner, Physical review B **47**, 558 (1993).

[48] G. Kresse and J. Furthmüller, Physical review B **54**, 11169 (1996).

[49] P. E. Blöchl, Physical Review B **50**, 17953 (1994).

[50] G. Kresse and D. Joubert, Physical Review B **59**, 1758 (1999).

[51] J. P. Perdew, K. Burke, and M. Ernzerhof, Physical Review Letters **77**, 3865 (1996).

[52] S. Plimpton, Journal of Computational Physics **117**, 1 (1995).

[53] A. Stukowski, V. V. Bulatov, and A. Arsenlis, Modelling and Simulation in Materials Science and Engineering **20**, 085007 (2012).

[54] A. Stukowski, Modelling and simulation in materials science and engineering **18**, 015012 (2009).

[55] B. Sadigh, P. Erhart, A. Stukowski, A. Caro, E. Martinez, and L. Zepeda-Ruiz,

Physical Review B **85**, 184203 (2012).

[56] J. Cowley, Physical Review **77**, 669 (1950).

[57] A. Ngan, Philosophical magazine letters **72**, 11 (1995).

[58] J. Chang, W. Cai, V. V. Bulatov, and S. Yip, Materials Science and Engineering: A **309**, 160 (2001).

[59] R. Peierls, Proceedings of the Physical Society **52**, 34 (1940).

[60] F. Nabarro, Proceedings of the Physical Society **59**, 256 (1947).

[61] L. Zhang, Y. Xiang, J. Han, and D. J. Srolovitz, Acta Materialia **166**, 424 (2019).